



New insights into nano-magnetism by spin-polarized scanning tunneling microscopy

Dirk Sander*, Hirofumi Oka, Marco Corbetta, Valeri Stepanyuk, Jürgen Kirschner

Max-Planck-Institut für Mikrostrukturphysik, Weinberg 2, D-06120 Halle/Saale, Germany

ARTICLE INFO

Article history:

Available online 1 October 2012

Keywords:

Nanomagnetism
Magnetization reversal
Electron spin polarization
Scanning tunneling microscopy

ABSTRACT

We study the magnetization reversal and the position dependence of the spin-dependent electronic properties of nm small bilayer Co islands on Cu(1 1 1) by spin-polarized scanning tunneling microscopy in magnetic fields at low temperatures of 8 K. The analysis of the energy barrier of magnetization reversal from measurements of the switching field suggests a crossover of the magnetization reversal mode with increasing island size around 7500 atoms from exchange-spring behavior to domain wall formation. The quantitative analysis of the island size dependence of the energy barrier indicates an inhomogeneous magnetic anisotropy of the island. The island rim is magnetically soft, whereas the center shows a pronounced effective anisotropy of 0.148 meV/atom. We speculate that this inhomogeneity of the magnetic anisotropy might be a consequence of the spatial dependence of the spin-dependent electronic properties. We measure a spin-polarization and a tunnel magneto resistance ratio of opposite sign at the rim as compared to the island center.

© 2012 Elsevier B.V. All rights reserved.

1. Introduction

At first sight the magnetization reversal of nm small structures seems to be well understood in nanomagnetism [1–3]. One is tempted to assume that as long as the particle dimensions are smaller than the width of a domain wall, reversal occurs by coherent rotation of all spins in a so-called macrospin model [4]. In the macrospin model, all spins of the structure are coupled by the exchange interaction, and the reversal can be described in the Néel–Brown model of thermally assisted reversal [5,6]. It is expected that in larger particles, magnetization reversal occurs by domain nucleation and growth, or by other reversal mechanisms. Note however, that in any case the macrospin description is a model, and more complicated reversal modes are conceivable [2,7–10].

Both fundamental research and applications show a tremendous interest in the understanding of the crossover between different reversal modes. This opens the way to modify the decisive parameters and to tune this transition as wished. A key parameter in this respect is the magnetic anisotropy energy density K . A large anisotropy favors stable magnetization directions against thermal agitation. This is required for example in magnetic data storage [11,12], where a sufficiently large ratio of the magnetic anisotropy

energy KV , V : volume of the magnetic entity, over the thermal energy $k_B T$ of order 60 is called for to ensure stable data storage.

However, the magnetic anisotropy changes dramatically when the dimensions of a particle are reduced to the nm scale in one or more dimensions. Lattice strain, its relaxation and the increasing relative number of surface and interface atoms induce a dramatic deviation of the magnetic anisotropy from its bulk values [13–17]. Also, structural [18,19] and electronic relaxations at the boundary of a nano structures [20] lead to distinct deviations of the atomic positions and the electronic structure on the nm scale. It is a priori not clear how the magnetic properties respond to this. Our work aims at providing experimental reference data for this largely unresolved issue.

To this end, we are striving for an understanding of the peculiar magnetic properties of a nanostructure on the electronic level. We exploit the unsurpassed spatial resolution of spin-polarized scanning tunneling microscopy [21–23] to investigate magnetization reversal and spin-dependent electronic properties of individual nano structures by scanning tunneling spectroscopy at low temperatures (8 K) in magnetic fields. In this work we focus on bilayer Co islands on Cu(1 1 1), which serve as a model system, as many structural [19], and electronic, including magnetic properties [20,24,25] have been established.

In Section 2 we address some experimental aspects of spin-polarized scanning tunneling microscopy. In Section 3 we present data on the magnetization reversal of individual bilayer Co islands on Cu(1 1 1). We find evidence for a spatial variation of the magnetic anisotropy, where the rim atoms of the Co islands are

* Corresponding author.

E-mail address: sander@mpi-halle.de (D. Sander).

magnetically soft. We reveal in a combined experimental and theoretical study the spatial variation of the spin-polarization and of the tunnel magneto resistance which we present in Section 4. These studies identify a pronounced difference in the electronic structure of the rim region as compared to the center region. In the outlook we speculate about the interplay between magnetic anisotropy and electronic structure near the rim region of Co islands.

2. Experimental aspects: spin-polarized scanning tunneling microscopy at low temperature in magnetic field and tips for its use

Scanning tunneling microscopy (STM) has developed into a powerful experimental technique to characterize magnetic nano structures over a wide size range from single atoms up to continuous films. Its strengths are manifold: atomic manipulation for the creation of artificial nano structures with atomic precision [26–28] and unsurpassed spatial resolution in imaging and spectroscopy on the atomic scale [29–31], including single spin excitation spectra [32].

The use of spin-polarized tips opens the way to characterize spin-dependent properties of nano structures by exploiting the dependence of the tunnel current $I(V)$ and of the differential conductance $dI/dV(V)$ on the relative orientation of the magnetization of tip and sample [21–23,33–35]. This technique is called spin-STM for short. By this technique, the spin-structure of antiferromagnetic surfaces [36,37] and of skyrmion lattices [38] has been resolved, and magnetic domain imaging [39,40] has been performed. Also, inelastic tunneling spectroscopy has been successfully applied to study magnons [41,42]. We note that also non-spin polarized tips have been discussed to reveal magnetic contrast as the electronic density of states above the sample surface depends on its magnetization state [43].

The strength of scanning tunneling spectroscopy is that the resulting data are related to the local electronic density of states of the tip-sample system [44,45], and this allows contact with calculation of the electronic density of states. Thus, a comparison between spin-dependent differential conductance measurements and calculated spin-resolved electronic density of states is possible and is applied in the discussion of the results in Section 4.

Still, there are some caveats when it comes to the application of spin-STM for magnetic characterization. Spin-STM is not a magnetometry technique. The link between the magnitude of the signal in spin-STM and the magnitude of the magnetic moments at tip and sample is not rigorously established. Presently it appears that micro-squid is the only technique capable of quantifying magnetic moments of individual nano structures [2]. Although the determination of the magnitude of the magnetic moment of a nano structure by spin-STM remains illusive, the relative orientation between the magnetization of tip and sample can be reliably established [46,47]. This requires an external magnetic fields to enforce a well defined magnetic reference state, which is often given by a parallel alignment of tip and sample magnetization at high magnetic fields. Therefore, spin-STM develops its full potential only in combination with sizable magnetic fields. Typically superconducting magnets are used to deliver fields of several T at the STM. This magnitude of magnetic field is typically required to manipulate the magnetization of nano structures and possibly that of the tip.

Note that also secondary electron microscopy with spin analysis (SEMPE) allows to image magnetic domains at surfaces [48–52]. It offers the benefit over spin-polarized scanning tunneling spectroscopy that it may give all components of the spin polarization of the secondary electrons emerging from the surface region of the nanostructure. The spatial resolution of SEMPE in the magnetic contrast mode is of order 5 nm [50]. A lateral resolution of order

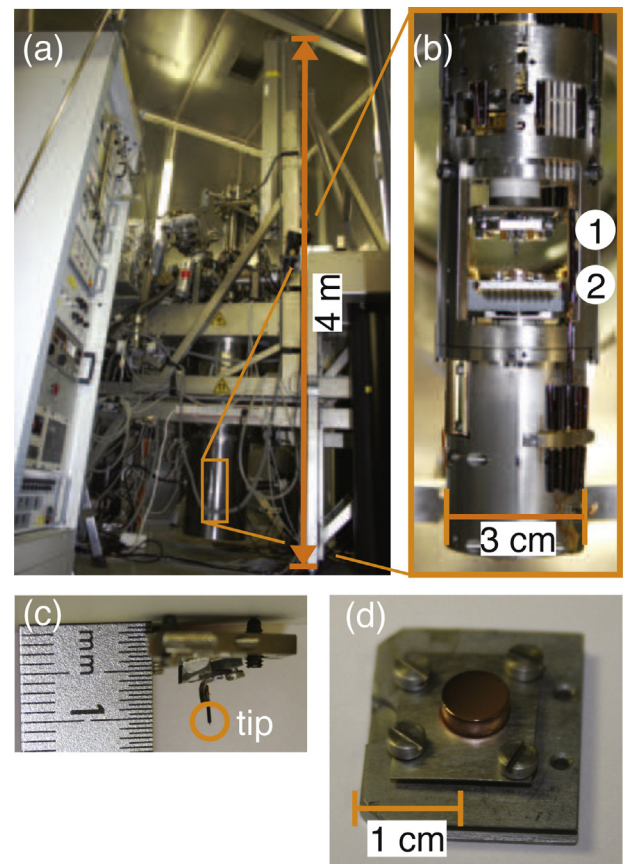


Fig. 1. (a) Side-view of Omicron cryogenic STM. The STM head (b) is located at the bottom end of the cryostat (orange rectangle). (b) The tip holder 1 mounted at the x , y coarse motion, the sample holder 2 is attached to the z -coarse motor and scanning piezo. (c) Side view of the tip holder, where the tip is spot welded to its support. (d) Cu(111) crystal, diameter 6 mm, mounted to the sample plate with Mo foils. (For interpretation of the references to color in this figure legend, the reader is referred to the web version of the article.)

10 nm in magnetic imaging is also possible by spin-polarized low energy electron microscopy, as described in Ref. [53].

2.1. LT-STM and superconducting magnet

Fig. 1 shows selected aspects of our low temperature STM with magnetic field [54]. The STM is a so-called top loader, where the STM head is lowered from the top into the cryostat. Loading of tip and sample into the STM is done in the UHV chamber above the cryostat at room temperature. The setup is fairly tall (4 m), as indicated in Fig. 1(a) to provide the necessary vertical travel.

The cryostat [55] contains concentric tanks for the cryo liquids. An outer liquid nitrogen surrounds an inner liquid helium (LHe) tank, which contains a superconducting magnet at its lower end. This magnet produces a magnetic field of up to 7 T along the vertical axis, normal to the sample surface. The STM is cooled by pressing the STM heat exchanger to a LHe cooled part within the UHV section of the cryostat by applying a contact force with the vertical lift. The lowest temperature is of order 7–8 K, as verified by calibrated sensors at the STM head.

Fig. 1(b) shows the STM head with the central opening for the insertion of tip (1) and sample holder (2). The tip can be positioned by a piezo coarse motion by ± 5 mm horizontally in x - and y -directions. The sample is mounted on the scanner piezo which gives a scan range of order $1 \mu\text{m}$ at 7 K. The scanner piezo is mounted at the z -coarse motion which gives a vertical travel of up to 10 mm.

The tip is spot welded to the tip holder Fig. 1(c), and the sample is clamped to a Mo-sample plate with thin Mo-foils Fig. 1(d).

The STM is combined with an UHV sample and tip preparation chamber, which includes a load lock for exchanging tip and sample without breaking the vacuum [56]. Tip and sample can be transferred from the preparation chamber into the STM by a magnetically coupled linear drive, using wobble sticks for tip and sample handling. There, tip and sample are prepared under UHV conditions. W-tips can be heated to 2400 K by electron beam heating to remove contaminants prior to the deposition of magnetic materials. E-beam evaporators allow to deposit Co, Cr, and Fe and combinations thereof under UHV conditions to prepare spin-polarized tips and samples. W-tips are electrochemically etched from a 0.5 mm wire prior to use. Bulk Cr tips are also used, and they do not need further UHV cleaning nor deposition of material in the preparation chamber. They also give magnetic contrast reliably [47].

The Cu(111) crystal is cleaned by cycles of Ar ion bombardment (1 keV, 1 μ A sample current, 10 min) at 300 K and subsequent annealing at 700 K for 10 min until atomically flat and clean large terraces (hundreds of nm wide) are obtained as checked in situ by STM at 300 K and after cool down to 8 K. Here we describe results on Co nano islands which are formed by Co deposition onto the clean Cu(111) crystal at 300 K with a deposition rate of order 2 min per monolayer.

In the following we focus on spectroscopy measurements of the differential conductance, so called $dI/dV(V)$ spectra [44,45]. In this mode of operation the tip-sample distance is stabilized at a gap voltage of +0.5 V and a tunnel current of 1 nA. We estimate that this leads to a tip-sample distance of order 0.4–0.5 nm. Then, the feedback loop, which controls the tip-sample distance to keep a constant tunnel current, is opened, and the gap voltage is swept from typically -1 to $+1$ V in some hundred steps within a few seconds. Simultaneously, the tunnel current $I(V)$ and the differential conductance dI/dV are measured. Typically, 10–20 scans are acquired to ensure a stable tip behavior and to improve the signal-to-noise ratio by averaging. The differential conductance is obtained from an AC modulation of the gap voltage with an amplitude of 10 mV at a frequency $f \approx 4$ kHz, and detecting the resulting modulation of the tunnel current at frequency f with a lock-in amplifier. These spectroscopy data characterize $I(V)$ and $dI/dV(V)$ at a single point. These measurements can be performed at each image pixel position, and a complete map of the spectroscopic properties results. The spectroscopic data acquisition of a 300×300 pixel image takes some 20 h. Low drift and low noise over this long data acquisition time are mandatory for this experiment. For comparison, a constant current image with simultaneously taken differential conductance value at a fixed gap voltage takes a few minutes.

2.2. Magnetic field response of tips in spin-STM

The working principle of the spin-STM relies on the use of spin-polarized tips. Typically, a W-tip is covered with several ten layers of a magnetic material to this end. Alternatively, bulk materials with a spin-polarization at the Fermi energy may also be used to obtain magnetic contrast. One needs to be aware of possible detrimental magnetic stray field effects when using bulk ferromagnets as tips. Stray fields can be minimized by using bulk antiferromagnets, such as Cr [47], as tip material.

However, even if the material at the tip apex is known to be spin-polarized as bulk sample, it is by no means a priori clear in which direction the magnetization at the tip apex points, nor how such a tip will respond to a magnetic field [57,47]. In the following we present examples of tips which were prepared by room temperature deposition of either 40 layer Cr, or by the subsequent

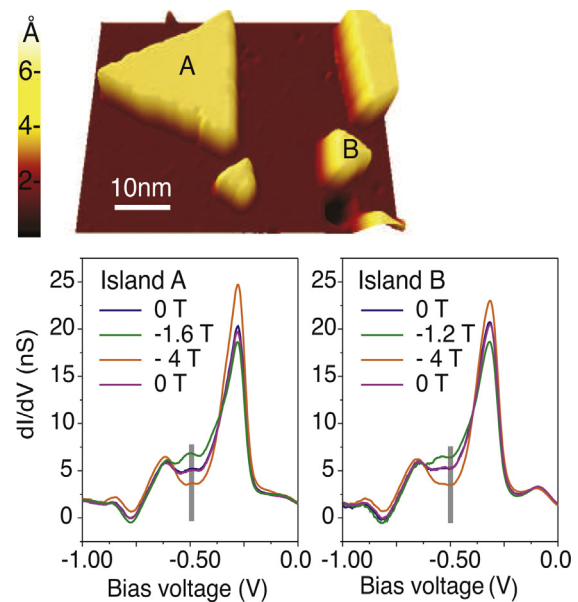


Fig. 2. 3D representation of a constant current image of bilayer high (0.4 nm) Co islands on Cu(111) and spectra of the differential conductance dI/dV measured at the center of islands A and B at different magnetic fields at 8 K with a 40 layer Cr/W-tip. The spectra change with field, and this indicates a change of the magnetic state of the system. The change with field depends on the bias voltage, and we plot its change at -0.5 V as a function of magnetic field in Fig. 3.

deposition of 40 layers Cr on 40 layers Co on a flashed W-tip. We demonstrate that in both cases the tips respond to the applied magnetic field. In the first case they respond by a smooth reorientation of the z-component of magnetization along the external field. In the second case, they exhibit a bistable behavior. The tip apex magnetization switches from up to down abruptly in response to the external field.

Fig. 2 shows the dependence of the differential conductance dI/dV on the magnetic field for measurements on two bilayer high Co islands A and B on Cu(111) with a 40 layer Cr/W-tip. The most prominent characteristic of the differential conductance dI/dV spectra is a peak near -0.3 V, which is ascribed to a Co minority state [58]. Changing the magnetic field induces changes of shape and amplitude of the dI/dV signal. Sign and magnitude of the signal change depend on the bias voltage. At bias voltages where the curves cross there is no effect of the magnetic field detectable. We choose a bias of -0.5 V to study the effect of the external field more clearly by plotting the differential conductance at -0.5 V as a function of field in Fig. 3. We do not select the bias at the peak position, as other mechanisms, such as position dependent structural relaxation [19], also induce significant variations of the differential conductance near -0.3 V, which might disguise the magnetic origin of the signal change.

We observe hysteresis curves of the differential conductance in Fig. 3, which are almost symmetric with respect to the y-axis. This finding tells us that both tip and sample respond to the magnetic field. The arrows in the small sketches indicate the magnetization direction of tip and sample. We see that the inner part of the hysteresis curves is identical for both curves, which have been taken with the same tip on a larger (island A) and a smaller (island B) Co island, which are identified in Fig. 2. The abrupt signal change at 1.6 and 1.2 T is ascribed to the magnetization reversal of the islands, which occurs at a larger field for the larger island. The smooth signal variation at smaller fields indicates a continuous increase of the z-component of the magnetization of the tip apex with increasing field. At large positive and negative fields the same differential

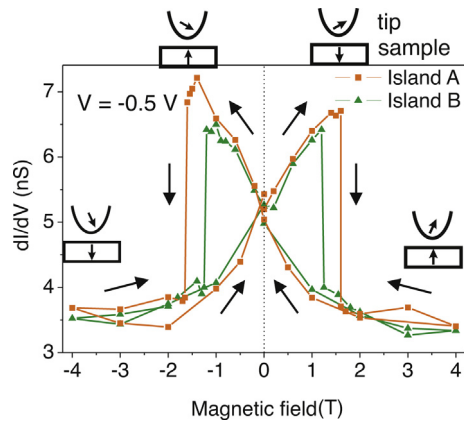


Fig. 3. Field dependence of the differential conductance at -0.5 V of Fig. 2 at 8 K. The symmetric hysteresis curves indicate that both tip and sample reorient in response to the magnetic field, as indicated by the sketches of the magnetization directions. The sharp signal drop indicates a reversal of the magnetization direction of the islands. The switching field is larger for the larger island A as compared to island B (1.6 T vs 1.2 T, respectively). The smooth signal variation at smaller fields indicates the orientation of the tip magnetization in field. The tip behavior can also be bistable, tip magnetization up or down, as shown for a Co/Cr/W tip in Fig. 4(c). Tip: 100 layers Cr/W-tip.

conductance is observed which indicates an equivalent magnetic state in view of the tunnel experiment.

Previous experiments have identified that the easy magnetization direction of bilayer Co islands on Cu(1 1 1) at low temperature is perpendicular to the surface with full remanence [24]. Thus our magnetic field triggers a magnetization reversal of the Co islands along the vertical direction. The observed field dependence of the differential conductance is compatible with the notion that the conductance of the tunnel junction depends on the relative orientation of the magnetization directions of both tip and sample. This is described by a theoretically founded $\cos(M_{\text{tip}}, M_{\text{sample}})$ dependence [59], where we take from previous magnetization studies that M_{sample} is collinear with the sample normal. The switching field of the sample depends on the Co island size in a nonmonotonic manner [60], as described in Section 3.

Fig. 4 presents an example, where a 40 layer Cr/40 layer Co/W-tip exhibits a bistable magnetic response. Here, the tip switches its magnetization orientation abruptly at ± 0.5 T. This is in sharp contrast to the hysteresis curve of Fig. 3, which indicated a smooth response of the tip apex magnetization orientation to the magnetic field. Here again we observe the same tip behavior at fields smaller than the switching field of the larger (A, 1.3 T) and smaller (B, 0.8 T) island. The corresponding variation of the tunnel current $I(V)$ is presented below in Fig. 12.

We refer to this hysteresis curve in our discussion of spatially modulated spin-dependent electronic properties in Section 4. There, we need to compare states of parallel (P) and anti-parallel (AP) magnetization orientation of tip and sample to extract information on the spin-polarization of the system. These states are clearly identified by the magnetic field sweep direction of the hysteresis cycle and are labeled in Fig. 4(c) as AP and P at -1.1 T.

In conclusion, magnetic tips may respond differently to the magnetic field. The distinction between the two tips is not meant to indicate that these tips will always show this behavior. Rather, the same macroscopic tip preparation may lead to drastically different magnetic field responses. This is possibly due to subtle and uncontrollable changes of the tip apex during scanning and operating the STM [47,57]. Critical aspects in this respect are the initial approach of the tip towards the sample when tunneling is established, unintended crashes of the tip with the surface while scanning, and the application of voltage pulses, which are commonly used to

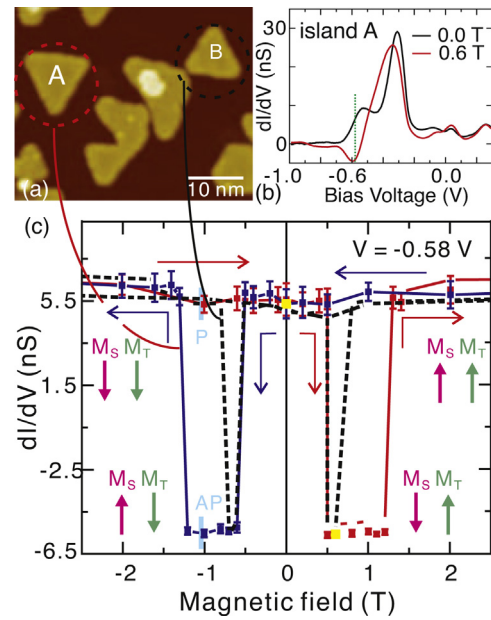


Fig. 4. Field dependent differential conductance with a bistable 40 layer Cr/40 layer Co/W-tip at 8 K. (a) Constant current image of bilayer high Co islands on Cu(1 1 1). (b) Differential conductance measured at the center of island A for parallel (0 T) and anti-parallel (0.6 T) magnetization alignment of tip and sample. The spectra differ mostly at -0.58 V, and the field dependence of the differential conductance at this bias is plotted in (c) for the island A (continuous line) and B (broken line). The sharp signal change at -0.5 T indicates the reversal of the tip magnetization, the sharp signal changes at larger fields than that of the islands. This tip has been used for the study of spin-dependent electron confinement in Section 4. The labels AP and P at -1.1 T identify anti-parallel and parallel alignment of tip and sample magnetization directions, respectively.

manipulate the tip apex. In spite of these obstacles, spin-polarized tips can be reliably characterized by the measurements of magnetic hysteresis cycles as demonstrated above and exploited in the magnetic characterization of nano structures discussed below.

3. Magnetization reversal of individual Co islands with thousands of atoms

The understanding of the magnetization reversal of nano structures is an outstanding problem both for fundamental research [2,10] and for application [11,12]. The quest for increasing storage density has spurred a lot of activity in this field, but an ab initio based description of the reversal process of structures with thousands of atoms and time scales of order 100 s is still beyond the present capabilities. Thus, experiments provide the required reference data to test models of magnetization reversal.

Such an experiment is presented here, where we study the magnetization reversal of individual bilayer high Co islands on Cu(1 1 1) at 8 K [60]. We have used Cr-covered W-tips, and also Cr/Co/W-tips as spin-polarized tips, where the individual film thickness was of order 100 atomic layers for Cr, and 40 atomic layers for Cr and Co each, respectively [57]. Previous experiments by spin-STM have established an easy out-of-plane magnetization of the islands with full remanence at zero field [24]. Our study provides quantitative data on the dependence of the switching field H_{sw} on island size. We extract the energy barrier ΔE of magnetization reversal from these data, and we find clear evidence for a crossover of the reversal mode from a coherent rotation of the inner part of the islands, which contributes to the magnetic anisotropy, to domain wall formation with increasing island size around 7500 atoms. The surprising aspect of this investigation is, that not all Co atoms contribute to the magnetic anisotropy. Our data suggests that the rim

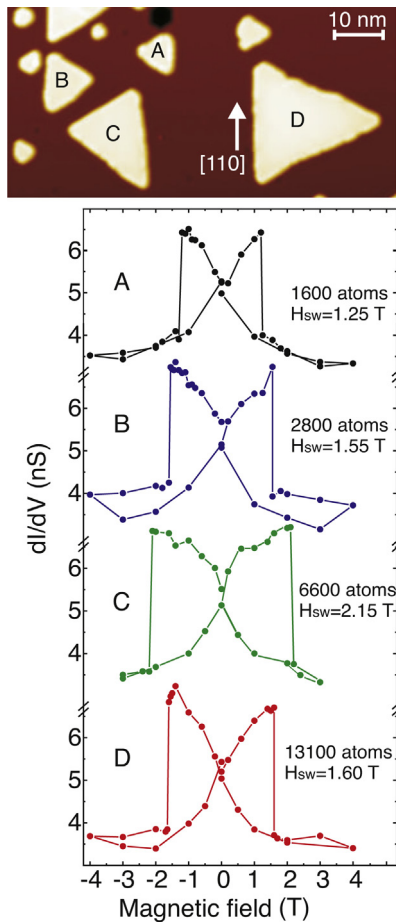


Fig. 5. Constant current image of several bilayer high Co islands on Cu(111) with corresponding hysteresis curves of the differential conductance at -0.5 V measured at 8 K in a magnetic field normal to the sample surface. The switching field H_{sw} and the island size in number of Co atoms is indicated at each curve.

atoms are magnetically soft. Thus, one may describe the Co nano islands as a one element exchange spring magnet. This sheds new light on the interplay between spatially dependent electronic and magnetic properties of nano scale objects, and this aspect is further elucidated in Section 4.

Fig. 5 shows a constant current STM image of bilayer high Co islands on Cu(111) together with a plot of the respective hysteresis curves of the differential conductance. The curves reveal a nonmonotonic dependence of the switching field on the island size. The switching field increases with island size for the smaller islands, and it reaches a maximum of 2.15 T for island C with 6800 atoms. It decreases to $H_{sw} = 1.6$ T for island with $N = 13,100$ atoms. This nonmonotonic dependence of H_{sw} on N is also apparent in the compilation of more data in Fig. 6. We find that the switching field increase with island size in regime 1 (blue), and it decreases in regime 2 (orange). The transition region is located around 7500 atoms.

The overall dependence of the switching field on island size is *qualitatively* readily understood. We observe the thermal assisted magnetization reversal of nano structures in regime 1 [6,61]. Small islands with less than a few hundred atoms show a superparamagnetic response at 8 K, and their switching field is zero. With increasing island size the magnetization is blocked on the time scale of our experiment (100 s), and a switching field is observed. The larger the island, the less important is the thermal agitation for the reversal, and the switching field increases sharply in regime 1 towards a value which is given by the Stoner–Wohlfarth model

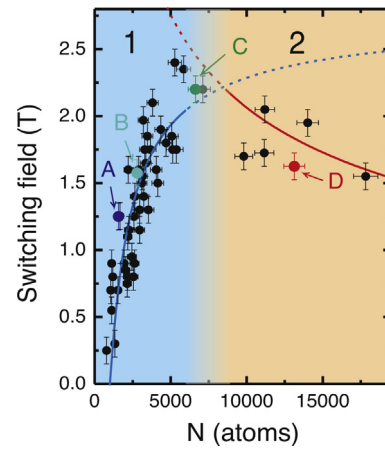


Fig. 6. Compilation of 54 switching fields of different bilayer Co islands on Cu(111) for measurements at 8 K. The labels identify the data of the islands of Fig. 5. The switching field increases with island size in regime 1 (blue), and it decreases in regime 2 (orange). (For interpretation of the references to color in this figure legend, the reader is referred to the web version of the article.)

$H_{max} = 2K/M$, where K is the effective anisotropy, and M the magnetization. However, with increasing islands size magnetization reversal by other mechanisms, such as domain nucleation and growth, becomes feasible, and the switching field decreases for larger islands. This characterizes the reversal in regime 2. Thus, regime 1 might characterize a magnetization reversal by coherent rotation of a macrospin, which changes to reversal by domain nucleation and growth in regime 2 for islands with more than ≈ 7500 atoms. This model of a transition from thermally assisted magnetization reversal of a macrospin to reversal by domain formation has already been described some 50 years ago in a study of the magnetization reversal of ensembles of FeCo alloy nano particles [61], and it appears tempting to apply it also here. However, our analysis reveals that this approach fails to describe the data *quantitatively*.

To elucidate the magnetization reversal quantitatively we extract the energy barrier ΔE of magnetization reversal from the switching field H_{sw} as

$$H_{sw} = \frac{2\Delta E}{N\mu} \left[1 - \left(\frac{k_B T}{\Delta E} \ln \frac{t_{meas}}{\tau_0} \right)^{1/2} \right], \quad (1)$$

with $\mu = 1.78\mu_B$ for the magnetic moment per Co atom, $\tau_0 = 10^{-10}$ s [2] and $t_{meas} = 100$ s, which reflects the time of one spectroscopy scan [60].

Fig. 7(a) shows the resulting compilation of the data on the energy barrier as a function of island size, where all switching fields plotted in Fig. 6 have been evaluated using Eq. (1). The curves through the data points represent fits where two different reversal mechanisms were considered. In regime 1 we fit a linear relation $\Delta E = K(N - N_0)$, in regime 2 $\Delta E = 4\sigma\sqrt{AK}$. The macrospin model of coherent rotation of *all* spins of the nano island in regime 1 requires a linear dependence of the energy barrier of the form $\Delta E = KN$. However, the data of Fig. 7(a) and the zoom in of (b) clearly show an offset at the x -intercept, which is mimicked by the inclusion of N_0 in the fit of regime 1. This suggests that a reduced number of atoms ($N - N_0$) contributes to the magnetic anisotropy. This is at variance with the expectation of a simple macrospin model discussed above, where all atoms contribute equally.

The fit in regime 2 considers an energy barrier of domain wall formation. The magnetic domain wall cross section is given by σ , and $A = 27.1$ meV/atom is the exchange interaction. The magnetic domain wall cross section is given by the thickness of the Co island (two atoms) times the geometric height, i.e. the distance

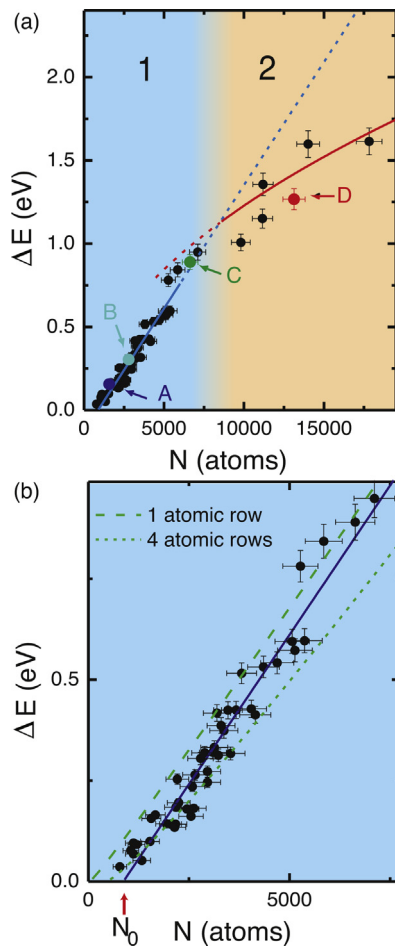


Fig. 7. (a) Calculated energy barrier ΔE from switching fields of Fig. 6. Labels identify the data of the islands of Fig. 5. The blue and the red line represent fits of the data where two different reversal mechanisms are considered. Magnetization reversal by coherent rotation in regime 1, and reversal by domain formation and growth in regime 2. The crossover between regimes 1 and 2 is given by the deviation from a linear dependence of the energy barrier on island size around 7500 atoms. (b) Zoom-in at regime 1. The data cluster along a linear solid curve, the same blue curve as shown in (a), which intersects the x-axis at N_0 (870 atoms). The broken curves show the result for $\Delta E = K(N - N_{rim})$, where N_{rim} is calculated for a 1 atom wide, and 4 atoms wide rim area, which is characterized by a vanishing anisotropy. The slope of the blue curve gives $K = 0.148 \pm 0.005$ meV/atom. (For interpretation of the references to color in this figure legend, the reader is referred to the web version of the article.)

from an island edge to an opposite corner, of the inner part of the island, which is extracted from the STM images. The magnetic anisotropy K is taken from the slope of the fit in regime 1, and we get $K = 0.148 \pm 0.005$ meV/atom. These two curves fit the experimental data in regimes 1 and 2 very favorably. We conclude that this analysis is a valid first step for the quantitative characterization of the reversal process at the nanoscale.

Note that K is the effective anisotropy. In view of the dipolar anisotropy for out-of-plane magnetization (-0.11 meV/atom) this suggest a magneto-crystalline anisotropy of 0.25 meV/atom (3.4 MJ/m³). This is roughly a factor 6 larger than the magnetic-crystalline anisotropy of bulk Co [16]. This reflects the decisive impact of the reduced dimensionality of the island on its enhanced anisotropy [16], where each atom is an interface atom.

The observation of an offset N_0 comes as a surprise. This offset can be interpreted as a number of atoms with vanishing anisotropy. To elucidate its physical origin, we plot in Fig. 7(b) also broken lines which consider that a rim region at each island of width 1 or 4 atoms

is magnetically soft. The plot indicates that the experimental data fall in between these limiting cases.

Thus we conclude that the Co islands show a region of vanishing magnetic anisotropy of width 1–4 atoms at their outer rim. We propose that the islands are magnetically inhomogeneous, where the rims show a behavior which deviates from the island center. The spatial variation of the magnetic properties might call for a quantitative analysis which goes beyond the coherent rotation model applied here. The impact of an inhomogeneous magnetic anisotropy on the nanometer scale on the magnetization reversal has been treated in atomic scale micro magnetic models for circular nano dots [62]. This work showed that a magnetically *hard* rim impacts the reversal mode. The authors revealed magnetization reversal by coherent rotation as a limiting case in small nano dots. Further work is called for to discuss the details of the reversal in view of the approximate triangular island shape and spatially varying magnetic properties, as we find it here. The next section discusses spatial variations of the spin-dependent electronic properties, and also there the rim area displays distinctively different properties from the center, which might be a clue for the electronic origin of the in-homogenous magnetic anisotropy.

4. Spatially modulated electronic properties on the nm scale of single Co islands

The lateral confinement of individual nm small islands leads to pronounced spatial variations of their electronic properties [20,58,63–66]. The impact of the lateral borders of the Co island on its electronic density of states is twofold. The reduced coordination of edge atoms in conjunction with electron spill out at the edge leads to a specific electronic state, the so-called rim state [20]. This state shows up in the spectroscopy of the differential conductance as a peak near the Fermi energy. This differs from the spectroscopy at the inner part of the island, which shows a characteristic peak near -0.3 V, but no pronounced feature near the Fermi energy, as displayed above in Fig. 2. Fig. 8 shows in the top part how the differential conductance signal changes near the rim. The rim state is observed for curves 2, 3, 4 and indicated near zero bias. The rim state is due to a modification of the electronic density of states *near the edge* of the island.

Fig. 8(b) and (c) shows maps of the differential conductance, which reveal a further characteristic position dependent electronic feature *in the center region of the island*. Here, the differential conductance signal is spatially modulated with a pattern, which reflects the symmetry of the island. This modulation is due to electron confinement [20]. The pattern can be ascribed to the formation of standing waves of the electronic density of states in the island surface, which is caused by scattering of electrons off the island boundaries [27,63]. Figs. 8(b) and (c) correspond to different magnetic states with anti-parallel (AP) and parallel (P) orientation of tip and sample magnetization, respectively [67]. The modulation patterns differ, and this difference is clearly displayed in the asymmetry image of the differential conductance, given in Fig. 8(d). The inner part shows a spatial modulation with a period which is determined by the electron dispersion relation of the Co island. The rim shows an opposite asymmetry and no distinct modulation.

The asymmetry of the differential conductance, $A_{dI/dV} = (dI/dV_{AP} - dI/dV_P) / (dI/dV_{AP} + dI/dV_P)$ is related to the spin-polarization of tip P_T and sample P_S as $A_{dI/dV} = -P_T P_S$ [22,67,68], and experimentally determined asymmetries of the differential conductance are presented in Figs. 8 and 10. The spin polarization above the Co island is calculated by finite functional theory in the multiple scattering Korringa–Kohn–Rostocker Green’s function method [67], and the result is presented in Fig. 9. Here, the spin polarization is determined from the asymmetry of the calculated

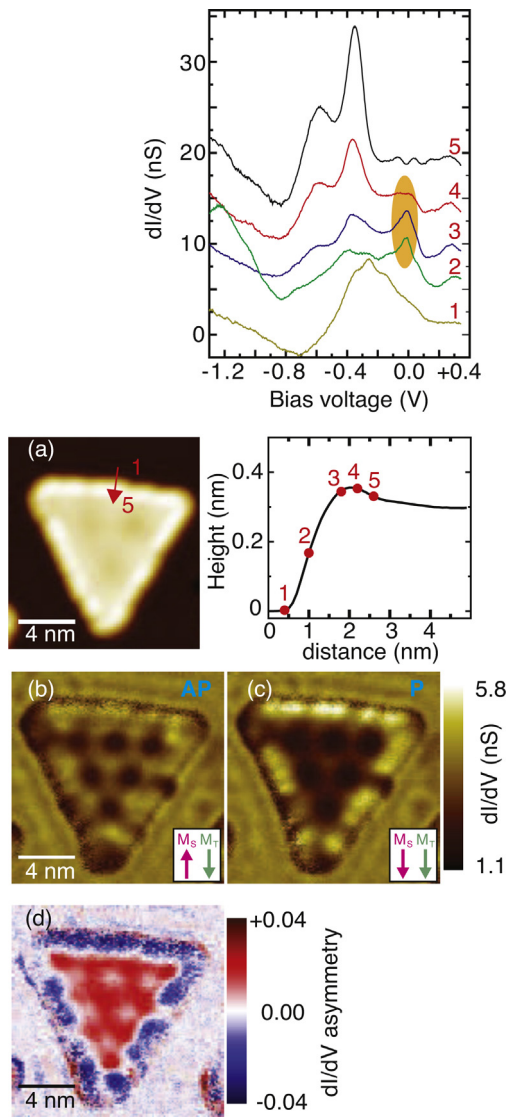


Fig. 8. Position dependent electronic properties of a single Co island. (a) Constant current image and linescan of a bilayer high Co island labeled A in Fig. 4. The top panel shows spectra of the differential conductance along the red arrow of (a). The rim state of spectra 2, 3, 4 near zero bias is indicated by the orange ellipse. The spectra are shifted vertically by 4 nS for clarity. (b) and (c) Map of the differential conductance at 0.03 V measured at -1.1 T at 8 K for anti-parallel (AP) and parallel (P) states, as indicated above in Fig. 4(c). (d) Calculated asymmetry map of the differential conductance by image math $(b - c)/(b + c)$. This asymmetry is related to the calculated spin-polarization shown in Fig. 9.

spin resolved density of states presented in maps Fig. 9(b) and (c) as $P_S = (n_{\uparrow} - n_{\downarrow})/(n_{\uparrow} + n_{\downarrow})$, where n_{\uparrow} and n_{\downarrow} are the calculated density of states above the Co surface for majority and minority states, respectively. These calculations show a pronounced spatial modulation of the density of states only for the majority channel. This finding is in agreement with the understanding that here majority states have a $s - p$ character of a free electron like surface state, which are susceptible to electron confinement. The constant density of states of minority states reflects that they are more localized due to their d -character [67,69].

The comparison between the experimental and theoretical results presented in Figs. 8(d) and 9(d) reveals striking similarities. We conclude that the asymmetry of the differential conductance is related to the spin polarization above the Co island. This relation between the experimentally accessible asymmetry of the differential conductance and the spin polarization is not limited

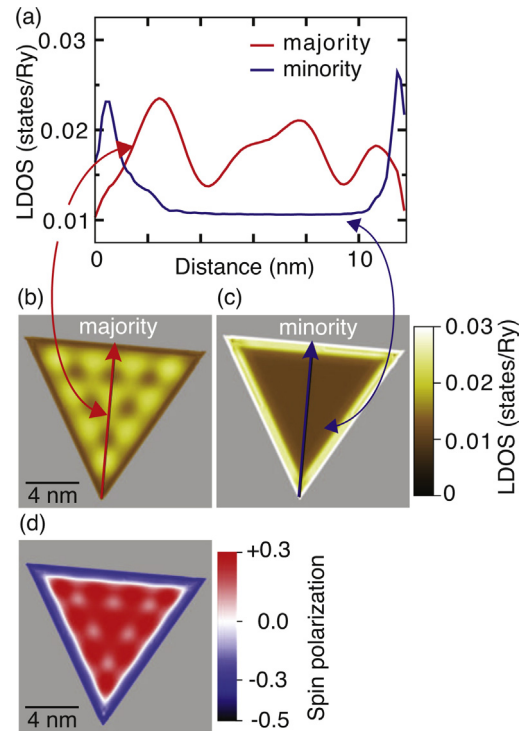


Fig. 9. (a) Calculated spin-resolved local density of states (LDOS) at the Fermi energy across the center line of a bilayer Co island 0.42 nm above the surface and map thereof for the majority (b) and minority states (c). Electron confinement induces a spatial modulation for majority states. (d) The calculated asymmetry $(b - c)/(b + c)$, which indicates a spatial modulation of the spin-polarization.

to the Fermi energy, as displayed in Figs. 8 and 9, but has been established over a wider energy range from -0.15 to +0.31 eV. This is apparent from the favorable similarity between experiment and theory presented in Fig. 10 [67]. These energy dependent studies indicate a non-monotonic change of the spin polarization above the center region of the island with increasing energy. Its physical origin is clarified by the calculations presented in Fig. 11. We see that the spin-resolved density of states changes differently with increasing energy for majority and minority states. This explains the variation of the spin-polarization with energy, where the difference of the density of states is exploited.

Further analysis supports the proportionality between the asymmetry of the differential conductance $A_{dI/dV}$ and the spin polarization P_S , where a proportionality constant of ≈ -0.1 reflects the spin polarization of the tip. This aspect is discussed in the supporting online material of reference [67].

We have demonstrated that the differential conductance and spin-polarization are spatially modulated due to spin-dependent electron confinement. We show in the next section that also the tunnel current and the tunnel magneto resistance ratio are modulated in the center part of the Co island for the same reason.

4.1. Spatially modulated spin-dependent transport properties

A spatial modulation of the spin-polarization of the sample is revealed in theory and observed experimentally in the asymmetry of the differential conductance. A spatial modulation of the spin polarization of the sample P_S is expected to also induce a spatial modulation of the tunnel current and of the magneto resistance. This conjecture is based on the assumption that the tunnel current I is also effected by the relative orientation of tip and sample magnetization, as discussed above for the

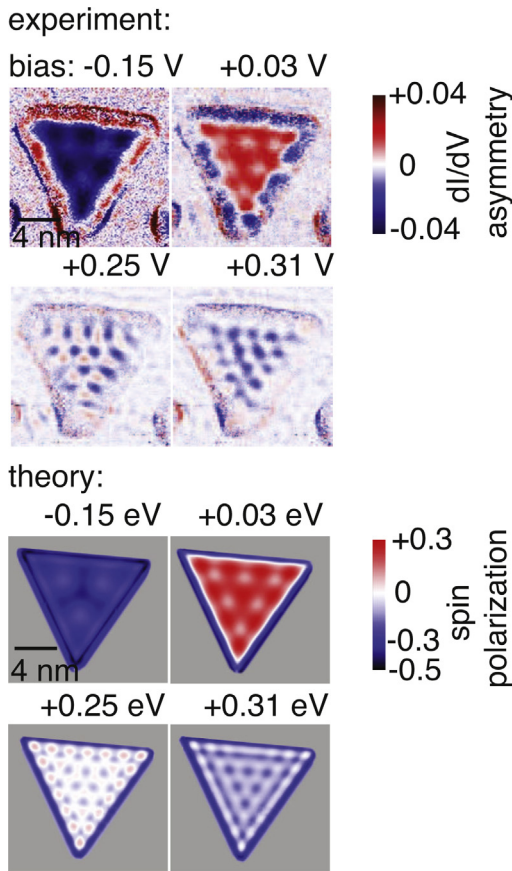


Fig. 10. Comparison between experimental asymmetry of the differential conductance and theory for the spin-polarization as a function of energy. Both experiment and theory show a contrast reversal with increasing energy of the center part of the island. Note the contrast reversal between -0.15 and $+0.03$ (eV). We find a contrast modulation around zero with positive and negative values (color code blue and red) at $+0.25$ (eV), whereas at $+0.31$ (eV) the modulation occurs within negative values only. This is ascribed to the energy-dependent difference of the minority and majority density of states, as presented in Fig. 11.

differential conductance. We obtain for the tunnel magneto resistance ratio $(R_{AP} - R_P)/R_P = (I_P - I_{AP})/I_{AP} = 2P_T P_S / (1 - P_T P_S)$ [22]. Thus, a spatial modulation of the sample spin-polarization P_S should also induce a spatial modulation of these transport properties, and it is indeed observed experimentally.

Experimentally we follow a similar procedure as above in Section 4. First, the hysteresis of the tunnel current is measured. Fig. 12(a) presents the dependence of the tunnel current on the magnetic state of the system. The tunnel current differs for parallel

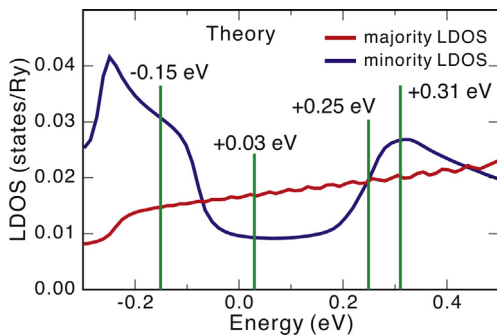


Fig. 11. Calculated spin-resolved density of states 0.42 nm above a bilayer high Co layer on Cu(111). The labels identify the energies of the sub-figures in Fig. 10. A larger majority density of states gives rise to a positive spin-polarization near the Fermi energy, as observed at $+0.03$ V.

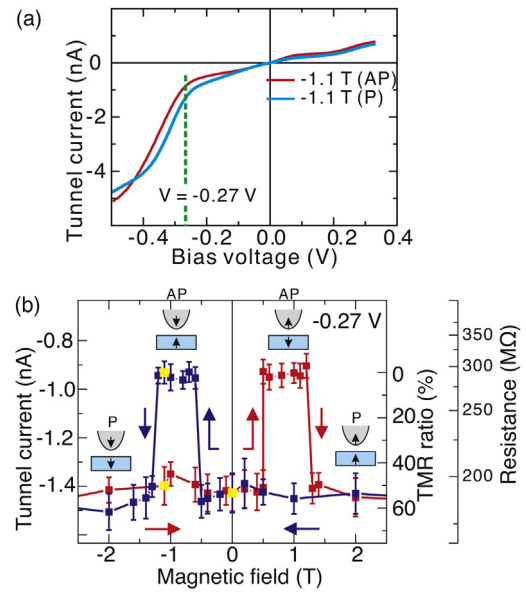


Fig. 12. (a) Spectrum of the tunnel current for anti-parallel (AP) and parallel (P) states measured above island A with the same tip as used in Fig. 4. Stabilization parameter $U = +0.5$ V, $I = 1$ nA, and $T = 8$ K. (b) Resulting hysteresis of the tunnel current. The tunnel magneto resistance (TMR) varies between 300 and 200 M Ω for AP and P states, respectively. The tunnel magneto resistance ratio $(R_{AP} - R_P)/R_P$ varies by 50%.

(P) and anti-parallel magnetization orientation of tip and sample. These data were collected simultaneously with the data of Fig. 4. Fig. 12(b) reveals the magnetic hysteresis of the tunnel current at a voltage, where Fig. 12(a) shows a pronounced dependence on the change of the magnetic state. This plot verifies that the tunnel current changes in response to the external magnetic field at the same field values as observed above for the hysteresis of the differential conductance.

We calculate the map of the tunnel magneto resistance ratio from maps of the tunnel current at parallel and anti-parallel magnetization states as $(I_P - I_{AP})/I_{AP}$ [70]. The result is shown in Fig. 13(a). The inner part of the island exhibits a spatial modulation of the tunnel magneto resistance ratio, the amplitude is of order 20%, as indicated by the linescan in Fig. 13(b). This ratio depends on the position within the island, and it changes with bias voltage. Fig. 13(c) plots the energy dependence of the tunnel magneto resistance ratio measured at the center position of the island. This experimental spectral dependence is well described in theory,

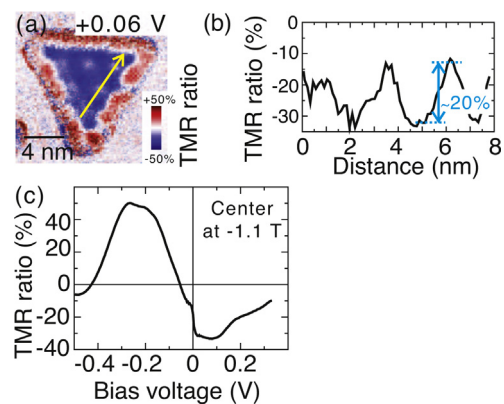


Fig. 13. (a) Map of the tunnel magneto resistance ratio measured at $+0.06$ V at 8 K on island A shown in Fig. 4. The line scan of (b) reveals a spatial modulation with an amplitude of order 20%. (c) Plot of the bias dependence of the tunnel magneto resistance ratio at the center of the island at -1.1 T.

which also delivers an understanding of the observed tunnel magneto resistance on the electronic level [70].

In conclusion, our study of the spatial dependence of spin-dependent electronic properties reveals pronounced differences between the center part of an island and its outer rim. It is striking that the apparent rim width in spin-dependent spectroscopy is of order one nm, and this is comparable to the proposed width of the magnetically soft rim above in Section 3. We speculate in the outlook below whether this might be taken as a hint for the electronic origin of the vanishing magnetic anisotropy near the rim as deduced from the switching behavior discussed above in Section 3.

5. Conclusion and outlook

We apply spin-polarized scanning tunneling microscopy in magnetic-fields to analyze the magnetization reversal of individual nm small bilayer Co islands on Cu(111) quantitatively. Within the Néel–Brown model of thermally assisted reversal we can describe our data in accordance with a crossover of the reversal process from exchange-spring behavior to domain wall formation with increasing island size around 7500 atoms. The analysis indicates that the rim atoms are magnetically soft, i.e. they show a negligible magnetic anisotropy, whereas the inner part of the islands is characterized by a considerable effective magnetic anisotropy of 0.148 ± 0.005 meV/atom. The width of the magnetically soft rim is deduced to be 1–4 atoms wide.

The high spatial resolution of the technique resolves spatial modulations of the asymmetry of the differential conductance and the tunnel current on the nm scale. In conjunction with theory we ascribe this to spin-dependent electron confinement which induces a spatial modulation of the spin polarization and of the tunnel magneto resistance of the inner part of the island.

What can we learn from the pronounced spatial dependence of the spin-polarization and of the tunnel magneto resistance ratio for the understanding of the magnetically soft island rim?

The observed spatial dependence of the electronic properties reflects the different electronic structure at the rim as compared to the center region. Our results indicate that the magnetic properties such as spin-polarization, tunnel magneto resistance and magnetic anisotropy vary sharply at the rim. Also, a previous combined experimental and theoretical study [19] has demonstrated how structural relaxations in Co islands modify their electronic structure. A clear understanding of the impact of electronic and structural relaxation and mesoscopic misfit [18] on magnetic anisotropy has not been established yet. We suspect that the pronounced spatial variation of the electronic structure within a single Co island is the key to an understanding of the resulting magnetic anisotropy. Future combined efforts in theory and experiment are called for to establish whether the similarity of the width of the rim region as observed in tunneling spectroscopy as compared to the estimate of the width of vanishing anisotropy from the analysis of the magnetic switching fields is of a related electronic origin.

The required theoretical effort is substantial. The local variation of all significant parameters, including structural and electronic relaxation, needs to be considered. The deduced large magnetic anisotropy of the center region of the island suggests that bulk properties do not serve as a reliable standard in these nm small Co bilayer structures, which are affected by a reduced coordination throughout the whole structure. The theoretical description of these single nanostructures is a formidable task in view of some thousands of atoms which need to be considered. It appears to be beyond current computational capabilities. Ultimately we strive for a theoretical description of all experimental aspects, where also the

magnetization reversal process can be described by theory [71–73]. Our results may contribute to this endeavor.

Acknowledgments

The authors acknowledge fruitful discussions with S. Ouazi, S. Wedekind, J. Borme, Y. Nahas, F. Donati, G. Rodary, L. Niebergall, P. Ignatiev, K. Tao and O. Brovko. We thank N. Kurowsky for expert technical support. Partial support by DFG SFB762 is gratefully acknowledged.

References

- [1] R. O'Handley, *Modern Magnetic Materials: Principles and Applications*, Wiley, New York, 2000.
- [2] W. Wernsdorfer, *Adv. Chem. Phys.* 118 (2001) 99.
- [3] R. Skomski, *J. Phys.: Condens. Matter* 15 (2003) R841–R896.
- [4] E.C. Stoner, E.P. Wohlfarth, *Philos. Trans. R. Soc. Lond. B: Biol. Sci.* 240 (1948) 599–642.
- [5] L. Néel, *Adv. Phys.* 4 (1955) 191–243.
- [6] W.F. Brown, *Phys. Rev.* 130 (1963) 1677–1686.
- [7] U. Nowak, O.N. Mryasov, R. Wieser, K. Guslienko, R.W. Chantrell, *Phys. Rev. B* 72 (2005) 172410.
- [8] D.A. Garanin, H. Kachkachi, *Phys. Rev. B* 80 (2009) 014420.
- [9] S. Rohart, P. Campiglio, V. Repain, Y. Nahas, C. Chacon, Y. Girard, J. Lagoute, A. Thiaville, S. Rousset, *Phys. Rev. Lett.* 104 (2010) 137202.
- [10] H.-B. Braun, *Adv. Phys.* 61 (2012) 1–116.
- [11] D. Weller, A. Moser, *IEEE Trans. Magnetics* 35 (1999) 4423–4439.
- [12] A. Berger, N. Supper, Y. Ikeda, B. Lengsfeld, A. Moser, E.E. Fullerton, *Appl. Phys. Lett.* 93 (2008) 122502.
- [13] D. Sander, A. Enders, C. Schmidthal, J. Kirschner, H. Johnston, D. Venus, *J. Appl. Phys.* 81 (1997) 4702–4705.
- [14] D. Sander, *Rep. Prog. Phys.* 62 (1999) 809–858.
- [15] S. Rusponi, T. Cren, N. Weiss, M. Epple, P. Bulusckek, L. Claude, H. Brune, *Nat. Mater.* 2 (2003) 546–551.
- [16] D. Sander, *J. Phys.: Condens. Matter* 16 (2004) R603–R636.
- [17] D. Sander, W. Pan, S. Ouazi, J. Kirschner, W. Meyer, M. Krause, S. Müller, L. Hammer, K. Heinz, *Phys. Rev. Lett.* 93 (2004) 247203.
- [18] O. Lysenko, V. Stepanyuk, W. Hergert, J. Kirschner, *Phys. Rev. Lett.* 89 (2002), 126102–1–126102–4.
- [19] M.V. Rastei, B. Heinrich, L. Limot, P.A. Ignatiev, V.S. Stepanyuk, P. Bruno, J.P. Bucher, *Phys. Rev. Lett.* 99 (2007) 246102.
- [20] O. Pietzsch, S. Okatov, A. Kubetzka, M. Bode, S. Heinze, A. Lichtenstein, R. Wiesendanger, *Phys. Rev. Lett.* 96 (2006) 237203.
- [21] W. Wulfhekel, J. Kirschner, *Appl. Phys. Lett.* 75 (1999) 1944–1946.
- [22] M. Bode, *Rep. Prog. Phys.* 66 (2003) 523.
- [23] R. Wiesendanger, *Rev. Mod. Phys.* 81 (2009) 1495–1550.
- [24] O. Pietzsch, A. Kubetzka, M. Bode, R. Wiesendanger, *Phys. Rev. Lett.* 92 (2004) 057202.
- [25] P.A. Ignatiev, V.S. Stepanyuk, *Phys. Rev. B* 84 (2011) 075421.
- [26] P. Zeppenfeld, C. Lutz, D. Eigler, *Ultramicroscopy* 42–44 (Part 1) (1992) 128–133.
- [27] M.F. Crommie, C.P. Lutz, D.M. Eigler, *Science* 262 (1993) 218–220.
- [28] S. Fölsch, P. Hyltdgaard, R. Koch, K.H. Ploog, *Phys. Rev. Lett.* 92 (2004) 056803.
- [29] R. Hamers, *Annu. Rev. Phys. Chem.* 40 (1989) 531–539.
- [30] J. Repp, G. Meyer, S.M. Stojković, A. Gourdon, C. Joachim, *Phys. Rev. Lett.* 94 (2005) 026803.
- [31] J. Repp, G. Meyer, S. Paavilainen, F.E. Olsson, M. Persson, *Science* 312 (2006) 1196–1199.
- [32] C.F. Hirjibehedin, C.P. Lutz, A.J. Heinrich, *Science* 312 (2006) 1021–1024.
- [33] M. Bode, M. Getzlaff, R. Wiesendanger, *Phys. Rev. Lett.* 81 (1998) 4256–4259.
- [34] A.R. Smith, R. Yang, H. Yang, A. Dick, J. Neugebauer, W.R. Lambrecht, *Microsc. Res. Technol.* 66 (2005) 72–84.
- [35] S. Rusponi, N. Weiss, T. Cren, M. Epple, H. Brune, *Appl. Phys. Lett.* 87 (2005) 162514.
- [36] S. Heinze, M. Bode, A. Kubetzka, O. Pietzsch, X. Nie, S. Blügel, R. Wiesendanger, *Science* 288 (2000) 1805–1808.
- [37] C.L. Gao, W. Wulfhekel, J. Kirschner, *Phys. Rev. Lett.* 101 (2008) 267205.
- [38] S. Heinze, K. von Bergmann, M. Menzel, J. Brede, A. Kubetzka, R. Wiesendanger, G. Bihlmayer, S. Blügel, *Nat. Phys.* 7 (2011) 713–718.
- [39] M. Pratzler, H.J. Elmers, M. Bode, O. Pietzsch, A. Kubetzka, R. Wiesendanger, *Phys. Rev. Lett.* 87 (2001) 127201.
- [40] E.Y. Vedmedenko, A. Kubetzka, K. von Bergmann, O. Pietzsch, M. Bode, J. Kirschner, H.P. Oepen, R. Wiesendanger, *Phys. Rev. Lett.* 92 (2004) 077207.
- [41] T. Balashov, A.F. Takács, W. Wulfhekel, J. Kirschner, *Phys. Rev. Lett.* 97 (2006) 187201.
- [42] C.L. Gao, A. Ernst, G. Fischer, W. Hergert, P. Bruno, W. Wulfhekel, J. Kirschner, *Phys. Rev. Lett.* 101 (2008) 167201.
- [43] M. Bode, S. Heinze, A. Kubetzka, O. Pietzsch, X. Nie, G. Bihlmayer, S. Blügel, R. Wiesendanger, *Phys. Rev. Lett.* 89 (2002) 237205.
- [44] W. Kaiser, R. Jaklevic, *IBM J. Res. Dev.* 30 (1986) 411–416.
- [45] G.A. Fiete, E.J. Heller, *Rev. Mod. Phys.* 75 (2003) 933–948.

- [46] G. Rodary, J.-C. Girard, L. Largeau, C. David, O. Mauguin, Z.-Z. Wang, *Appl. Phys. Lett.* 98 (2011) 082505.
- [47] M. Corbetta, S. Ouazi, J. Borme, Y. Nahas, F. Donati, H. Oka, S. Wedekind, D. Sander, J. Kirschner, *Jpn. J. Appl. Phys.* 51 (2012) 030208.
- [48] H. Oepen, R. Frömter, Scanning electron microscopy with polarization analysis, in: *The Handbook of Magnetism and Advanced Magnetic Materials*, vol. 3, Wiley, New York, 2007.
- [49] S. Hankemeier, R. Frömter, N. Mikuszeit, D. Stickler, H. Stillrich, S. Pütter, E.Y. Vedmedenko, H.P. Oepen, *Phys. Rev. Lett.* 103 (2009) 147204.
- [50] T. Kohashi, M. Konoto, K. Koike, *J. Electron Microsc.* 59 (2010) 43–52.
- [51] R. Frömter, S. Hankemeier, H.P. Oepen, J. Kirschner, *Rev. Sci. Instrum.* 82 (2011) 033704.
- [52] F. Lofink, S. Hankemeier, R. Frömter, J. Kirschner, H.P. Oepen, *Rev. Sci. Instrum.* 83 (2012) 023708.
- [53] N. Rougemaille, A.K. Schmid, *Eur. Phys. J. – Appl. Phys.* 50 (2010) 20101.
- [54] Omicron Nanotechnology. www.omicron.de, 2005.
- [55] Janis Research Company. www.janis.com, 2005.
- [56] H. Oka, G. Rodary, S. Wedekind, P.A. Ignatiev, L. Niebergall, V.S. Stepanyuk, D. Sander, J. Kirschner, *Spintronics IV* 8100 (2011) 810000.
- [57] G. Rodary, S. Wedekind, H. Oka, D. Sander, J. Kirschner, *Appl. Phys. Lett.* 95 (2009) 152513.
- [58] L. Diekhöner, M.A. Schneider, A.N. Baranov, V.S. Stepanyuk, P. Bruno, K. Kern, *Phys. Rev. Lett.* 90 (2003) 236801.
- [59] D. Wortmann, S. Heinze, P. Kurz, G. Bihlmayer, S. Blügel, *Phys. Rev. Lett.* 86 (2001) 4132–4135.
- [60] S. Ouazi, S. Wedekind, G. Rodary, H. Oka, D. Sander, J. Kirschner, *Phys. Rev. Lett.* 108 (2012) 107206.
- [61] E.F. Kneller, F.E. Luborsky, *J. Appl. Phys.* 34 (1963) 656–658.
- [62] S. Rohart, V. Repain, A. Thiaville, S. Rousset, *Phys. Rev. B* 76 (2007) 104401.
- [63] J. Li, W.-D. Schneider, R. Berndt, S. Crampin, *Phys. Rev. Lett.* 80 (1998) 3332–3335.
- [64] J. Kliewer, R. Berndt, S. Crampin, *New J. Phys.* 3 (2001) 22.
- [65] S. Pons, P. Mallet, J.-Y. Veuillen, *Phys. Rev. B* 64 (2001) 193408.
- [66] I. Barke, H. Hövel, *Phys. Rev. Lett.* 90 (2003) 166801.
- [67] H. Oka, P.A. Ignatiev, S. Wedekind, G. Rodary, L. Niebergall, V.S. Stepanyuk, D. Sander, J. Kirschner, *Science* 327 (2010) 843–846.
- [68] J.C. Slonczewski, *Phys. Rev. B* 39 (1989) 6995–7002.
- [69] L. Niebergall, V.S. Stepanyuk, J. Berakdar, P. Bruno, *Phys. Rev. Lett.* 96 (2006) 127204.
- [70] H. Oka, K. Tao, S. Wedekind, G. Rodary, V.S. Stepanyuk, D. Sander, J. Kirschner, *Phys. Rev. Lett.* 107 (2011) 187201.
- [71] A. Sukhov, J. Berakdar, *J. Phys.: Condens. Matter* 20 (2008) 125226.
- [72] D.S.G. Bauer, P. Mavropoulos, S. Lounis, S. Blügel, *J. Phys.: Condens. Matter* 23 (2011) 394204.
- [73] D. Böttcher, A. Ernst, J. Henk, *J. Phys.: Condens. Matter* 23 (2011) 296003.